Quantum dynamics of secondary electron emission from nanographene

Yoshihiro Ueda, Yasumitsu Suzuki, and Kazuyuki Watanabe*
Department of Physics, Tokyo University of Science, 1-3 Kagurazaka, Shinjuku-ku, Tokyo 162-8601, Japan
(Received 24 March 2016; revised manuscript received 25 May 2016; published 5 July 2016)

We have observed secondary electron emission (SEE) from nanographene by applying time-dependent density functional theory simulations in real-time and real-space to electron scattering on target graphene-flakes. We obtained the incident-electron energy dependence and bilayer effect on the amount of secondary electron (SE). The dynamics of SEE and collective density oscillations, which are electronic excitations induced by electron impact, were demonstrated numerically, and elucidated by the time-dependent occupation numbers of the Kohn-Sham electronic levels. The SE yields from graphene flakes are found to be ∼0.1. The highest energy of SE is ∼20 eV, which is compatible with the characteristics observed in SEE experiments.

DOI: 10.1103/PhysRevB.94.035403

Since the discovery of secondary electron emission (SEE) in 1902 [1], SEE has been well studied experimentally. The electrons that are emitted from the target when high-energy electrons of ∼keV are incident on a target material are called secondary electrons (SEs). Generally, an SE emitted from target materials has a low energy <50 eV, so SE is distinguished from a primary (incident) electron by the energy spectrum. Research in this area has developed the technology for SEE applications [2–5]. Especially, scanning electron microscopy (SEM) is a very valuable and useful technique that applies SEE to obtain information about surface structures. This has been applied recently to observe Å-scale atomic structures [6].

Monte-Carlo (MC) simulations with empirical models are used widely for the theoretical study of SEE. For example, MC simulations explain well the incident-energy and angle dependence of secondary electron yields (SEY) [7,8]. The MC simulations, however, are performed under various approximations, such as a flat jellium surface instead of a crystal surface, the first-Born approximation for scattering processes, etc. [7,9]. The jellium model neglects Å-scale atomic structures and the first-Born approximation is not suitable for simulations with a low incident-energy that is comparable to the Fermi energy of the targets.

Thus, we have carried out a first-principles theory simulation of SEE of low-dimensional materials. We chose nanographene as the target material in the present study, because graphene, as a representative material for low-dimensional materials, has attracted considerable interest because of its atomic, electronic, magnetic, and optical properties [10], and because graphene is a simple and ideal target to elucidate the mechanism underlying SEE. The amount of SE from nanographene is hard to evaluate experimentally, because SEE from graphene and its substrate are indistinguishable [11,12]. In addition, reliable experiments are rare at an incident energy <100 eV, because the backscattered electrons and secondary electrons have comparable energy and become indistinguishable [7,13]. Therefore, the MC simulations for SEE are no longer valid for the real surfaces of atomic sheets and the case of low incident energies. To complete the understanding of SEM images and to further develop the techniques, we need to establish a simulation method to overcome these problems and to elucidate the mechanism of SE generation from first principles.

In our recent study, we used time-dependent density functional theory (TDDFT) [14–16] for the simulation of nanoscale low-energy electron diffraction patterns of graphene flakes [17]. TDDFT is a formally exact method that treats the full dynamic processes of both the target and incident electrons simultaneously. Zhang *et al.* [18] successfully applied the TDDFT scheme to the study of SEE upon helium-ion scattering with graphene as a simulation of helium ion microscopy. Here, we inject an electron instead of an ion into the graphene flakes. We numerically demonstrate electron scattering with graphene flakes and reveal the levels of SEE by TDDFT in a real-time and real-space scheme. The microscopic mechanism of SEE is elucidated by the calculations of incident-energy dependence, layer-number dependence, and the time-dependent electron occupation number of the target.

When treating electron scattering with a target, we first determined the ground state of the target by density functional theory [19,20] and the initial state of a free electron by a Gaussian wave packet (WP). Then the whole system is propagated in time by TDDFT. The one-body wave functions $\psi_j(\mathbf{r},t)$ that belong to the target and $\psi_{\rm wp}(\mathbf{r},t)$ that belongs to the incident projectile at $t = 0$ evolve in time according to the time-dependent Kohn-Sham (TDKS) equation

$$i\frac{\partial}{\partial t}\psi_k(\mathbf{r},t) = H_{\rm KS}[n(\mathbf{r},t)]\psi_k(\mathbf{r},t), \tag{1}$$

$$n(\mathbf{r},t) = 2\sum_{j=1}^{N/2}|\psi_j(\mathbf{r},t)|^2 + |\psi_{\rm wp}(\mathbf{r},t)|^2, \tag{2}$$

where k runs from 1 to $N/2$ and "wp", N is the number of electrons in the target, and the system is assumed to be spin unpolarized. The "wp" is the state index of the wave packet (see Ref. [17] for the details). The incident electron gradually interacts with target electrons as it approaches the target; therefore, both wave functions become perturbed as time increases. Here, the interaction between the two electron subsystems is not exact in that it does not include the exact exchange-correlation potential but an approximated one in the sense of ALDA. Both electrons of the target and wave

*kazuyuki@rs.kagu.tus.ac.jp

packet experience the same Kohn-Sham potentials that are the functional of total electron density [Eq. (2)], and both wave functions are heavily disturbed and mixed upon electron impact, so that the target and wave packet electrons are no longer distinguishable. We adopt atomic units throughout the paper, unless stated otherwise.

We calculated the time evolution of Kohn-Sham decomposition, expressed by

$$M_i(t) = 2\sum_{j=1}^{N/2} |\langle\psi_i(0)|\psi_j(t)\rangle|^2 + |\langle\psi_i(0)|\psi_{\rm wp}(t)\rangle|^2, \quad (3)$$

to reveal the excitation dynamics of the target electrons upon electron impact. Here i runs through all the levels obtained in the KS ground state, j runs from 1 to $N/2$. Here, $M_i(t)$ indicates the number of electrons that belong to an energy level i in the ground state, i.e., it is a time-dependent occupation number. At $t = 0$, M_i is two for $i \leqslant N/2$ and zero for $i > N/2$. We note that what is typically obtained experimentally is the current (or kinetic energy) spectrum of the emitted electrons, and it is not the same quantity as that calculated by Eq. (3). However, we have found that our Kohn-Sham decomposition scheme does reproduce the spectral characteristics obtained experimentally. We also note that there are other approaches to calculate the energy spectra of emitted electrons using real-time TDDFT [21,22]. For example, Fourier transforms (FT) of the time-dependent Kohn-Sham orbitals would give the kinetic-energy spectra of electrons directly [21], though it requires a longer computational time than in the present study to obtain the spectra in the low-energy (<10 eV) region.

A schematic view of the WP-target system is shown in Fig. 1. The calculation box is $20.6 \times 20.6 \times 31.7$ Å^3. A target graphene flake is placed in the center of the box, i.e., on the xy plane at $z = 0$, and the propagating WP is shot along the direction perpendicular to the flake plane from the positive z region. Because we adopted the boundary condition that the wave function is zero at the boundary of the calculation box, the target is a finite-sized graphene flake [$C_{54}H_{18}$: circumcoronene shown in the inset of Fig. 1(b)]. We used the kinetic energy $E_{\rm kin} = \mathbf{k}^2/2 = 50\sim600$ eV and the width 1.1 Å for the incident WP. The initial distance, 6.35 Å of WP from the target plane is large enough that there is no overlap between the wave functions. The time evolution of the KS wave functions was explored by a fourth-order Taylor expansion method [23]. The norm-conserving pseudopotential [24,25] and the adiabatic local-density approximation (ALDA) [26] for the exchange-correlation interaction were also used. We used a time step $\Delta t = 2.42 \times 10^{-4}$ fs and a grid spacing 0.16 Å. During the simulation, the atomic positions are fixed because the time interval is too short to see the atomic motion. The area surrounded by dashed lines, which are 4 Å away from the target, is defined as the flake area. Complex absorbing potentials (CAP) [27,28], which are 4.8 Å wide, are placed at both ends of the calculation box. The electrons entering CAP disappear quickly. Figure 1(b) shows the time evolution of the electric current in the direction of z calculated by $\psi_{\rm wp}(\mathbf{r},t)$ upon scattering with monolayer circumcoronene (at the center of the horizontal axis). Almost all of the components of $\psi_{\rm wp}(\mathbf{r},t)$ transmit through, and a small fraction reflects off the target.

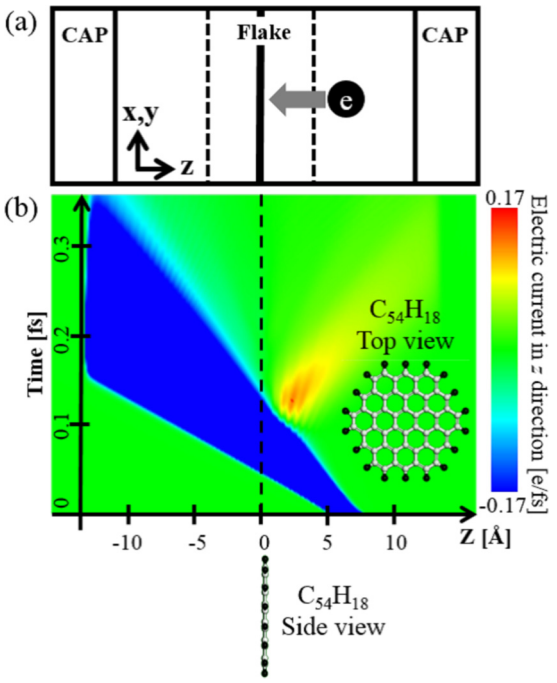

FIG. 1. (a) Schematic view of the calculation box. The target flake is at the center of the box. The initial position of WP is 6.35 Å away from the target. The area surrounded by dashed lines is defined as the flake area. Complex absorbing potentials (CAP) are placed on both ends. (b) Time-space mapping of electric current of $\psi_{\rm wp}(\mathbf{r},t)$ upon scattering with a monolayer target. The red (and yellow) region shows positive current and the blue region shows negative current. The horizontal axis is the z axis defined in (a). The vertical axis is time. The dashed line denotes the target position. The atomic structure of the target ($C_{54}H_{18}$) is given in the inset. The white and black balls correspond to carbon and hydrogen atoms, respectively.

We make a few comments on the method used in this study. We applied TDDFT to the real-time simulation of the electron-scattering process. It is known as one of the most challenging issues of TDDFT [29–32], because an exchange-correlation potential that takes into account the derivative discontinuity [33,34] and universal dynamical steps [35] is desirable to treat such a highly correlated two-electron process. Here, as a first study of the real-time SEE simulation, we employed ALDA and demonstrated how it works. Of course, a more accurate exchange-correlation functional could be taken into account by adopting, e.g., the time-dependent optimized effective potential approach [36–38].

Let's present the simulation results. The results for the time evolution of electron numbers in the flake area for the incident electron-WP of various kinetic energies are shown in Fig. 2(a). The electron numbers increase from 234, which is the valence-electron number of $C_{54}H_{18}$, by almost one and then immediately decrease back to 234 again and even lower for higher kinetic energies. The electron deficit (compared to 234) in the flake area is evidently the signature of SEE. The amount of SE becomes nearly 0.1 for a kinetic energy of 600 eV. Regarding the influence of the CAP, we checked the influence on the amount of SE by performing a simulation with the CAP moved outwards by 8 Å from the original position and found the change of $\sim10^{-3}$, i.e., negligibly small.

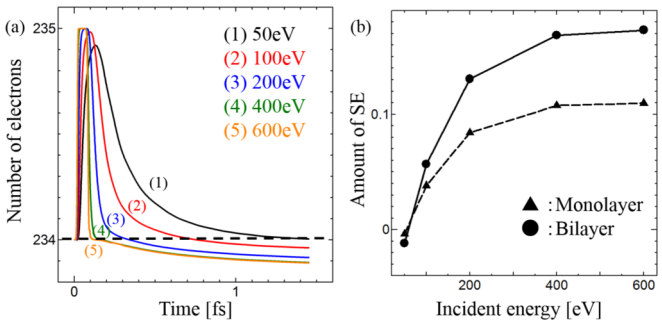

FIG. 2. (a) Time evolution of the electron number in the flake area defined in Fig. 1(a). The time is set to zero when WP is injected at the initial position. The target $C_{54}H_{18}$ has 234 electrons and the WP one at $t = 0$. The five curves show the time-dependent electron numbers upon electron impact with different incident kinetic energies. (b) Incident-energy dependent SEE from monolayer (dashed line with triangles) and bilayer (with a gap of 3.4 Å) graphene flakes (solid line with dots). The values depicted are the deficits in the electron numbers at $t = 1.5$ fs in (a). The amounts become negative at 50 eV, because a fraction of the incident electron is still inside the flake area at $t = 1.5$ fs.

The amount of SE at $t = 1.5$ fs in Fig. 2(a) is depicted as a function of incident kinetic energy together with that of bilayer graphene flake in Fig. 2(b). The SEEs increase in the low-energy region and level off beyond ∼400 eV. Although there are no simulations for kinetic energies higher than 600 eV, we naturally predict that the SEE decreases with a further increase in the incident energy, because the time interval of interaction between the faster incident electron and the electrons in the target decreases. As a result the probability of SEE decreases [39].

The SEE from the bilayer (solid line) is found to be less than twice that from the monolayer (dashed line), which is physically reasonable. The primary reasons are the following: The electrons incident at the second layer that are transmitted from the first layer have lower energy than the electrons incident on the first layer. Thus, the transmittance of the electrons through the second layer decreases from that through the first layer. The secondarily emitted electrons that propagate toward the negative direction from the first layer and toward the positive direction from the second layer are intercepted by the second layer and first layer, respectively. The additional reason, which is a finite size effect and numerically small, is that a fraction of the electrons transmitted or secondarily emitted from the first flake does not enter, but bypasses the second flake instead of generating SE.

Next, we investigate the electron-impact induced electronic excitations of the target. The spatiotemporal current distribution around the monolayer graphene upon electron impact of kinetic energy 200 eV is shown in Fig. 3(a). The blue and red patterns launching from the bottom indicates SEE toward negative and positive directions in the z axis, respectively. The repetition in time of the blue and red spots in the flake indicates the current oscillation normal to the flake plane. The period of the current oscillation is found to correspond to an energy of ∼16 eV. Although the current oscillation is along the direction normal to the target layer, the energy is close

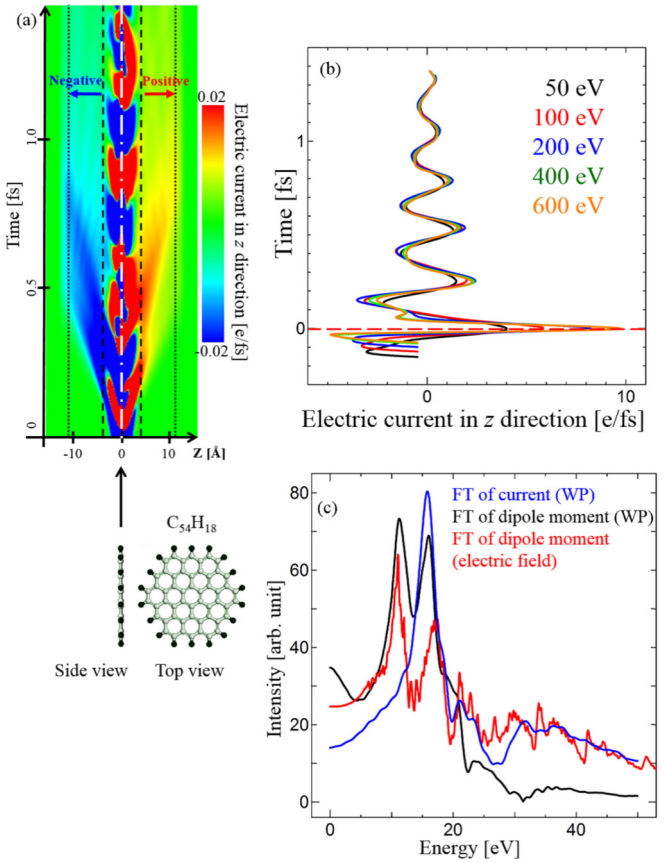

FIG. 3. (a) Spatiotemporal current distribution around monolayer graphene upon electron impact of kinetic energy 200 eV. The vertical axis is time (0 ∼ 1.5 fs) and the horizontal axis is the z axis defined in Fig. 1(a). The flake is placed at the center (white line), the flake area is surrounded by dashed lines, and the CAP regions are separated from the scattering region by dotted lines. The blue and red patterns indicate the negative and positive currents, respectively, of $\psi_1(\mathbf{r},t) \sim \psi_{N/2}(\mathbf{r},t)$ integrated over the x and y directions [see Fig. 1(a)]. (b) Time evolution of the current on the target [white line in (a)]. The five curves show the currents for different incident energies. They were shifted to align with the first peak position at $t = 0$. (c) Fourier transforms (FT) of the current, $j_z(\omega)$ (blue line) and dipole oscillation, $p_z^{\mathrm{wp}}(\omega)$ (black line) upon electron impact of 200 eV incident energy. Red line shows the dipole excitation induced by an external optical electric field with a δ-function form, $p_z^{\mathrm{E}}(\omega)$.

to 15 ∼ 16 eV of the π-σ plasmon (layer-parallel mode) that were numerically confirmed to exist in the photoabsorption spectra in a previous study [40]. More importantly, this oscillation period remains unchanged by changing the incident kinetic energy of the electron impact, as shown in Fig. 3(b). It supports the idea that this oscillation corresponds to one of the electronic excitation intrinsic to the target. Furthermore the amplitude of this oscillation (∼16 eV) also remains unchanged for different incident kinetic energies. Thus it is considered not to be the main origin of the SEE, because the amount of SE is dependent on the incident kinetic energy. We also note that the current oscillation in Fig. 3(b) attenuates in time. Although the mechanism for the decay is not yet clear, a similar damping phenomenon has been observed and interpreted as the result of the elastic scattering of electrons with ionic core

potentials in a previous study [41] where the TDDFT was used with a pseudopotential framework similar to the present case.

To discuss this electron-impact induced electronic excitation more clearly, we have calculated the FTs of the current oscillation, $j_z(\omega)$ [shown as a blue curve in Fig. 3(c)], the dipole excitation induced by the same electron wave packet impact, $p_z^{\mathrm{wp}}(\omega)$ [black curve in Fig. 3(c)], and the dipole excitation induced by an external optical electric field with a δ-function form [17,23,40], $p_z^{\mathrm{E}}(\omega)$ [red curve in Fig. 3(c)]. First, the similarity between the black and red curves is recognized. Both curves have two peaks at around 12 eV and 16 eV. This similarity can be understood by the fact that the incident electron applies an electric field to the target, and its effect can be regarded as similar to that of white light [42]. Thus, the dipole excitation normal to the plane has been induced by the electron impact. Since $j_z(\omega)$ has a peak at $\sim$16 eV, which is similar to those of $p_z^{\mathrm{wp}}(\omega)$ and $p_z^{\mathrm{E}}(\omega)$, the current oscillation in Figs. 3(a) and 3(b) is also interpreted as the dipole oscillation in the direction normal to the plane. We consider that the absence of the second peak at $\sim$12 eV in $j_z(\omega)$ is associated with the different symmetry of the current in space from those of the dipole moments. In addition, we cannot presently conclude if the present oscillation has relevance to the π-σ plasmon excitation that is normal to the plane. However, the intersubband plasmons in a two-dimensional quantum well that has oscillations in the direction normal to the plane has been discussed using TDDFT calculation [43]. Therefore, future investigation of this issue would be intriguing with respect to charge impact-induced nanoplasmon excitation.

Next, we extract the SEE electronic-states origin from the time-dependent occupation numbers of the Kohn-Sham (KS) levels (KS decomposition scheme) defined in Eq. (3). A snapshot of the electron occupation numbers of the target at $t = 1.5$ fs after electron impact with a kinetic energy of 200 eV is given in Fig. 4(a). The blue and red dots denote, respectively, the occupation numbers in the occupied and unoccupied KS levels that are separated by the HOMO-LUMO gap. From the variation in the occupation numbers with energy, we find that the electron impact exerts substantial and complex influence on the electronic states.

To check the number conservation accurately, we repeated the simulation by replacing $C_{54}H_{18}$ with a benzene molecule C_6H_6, and we confirmed that the sum of the total number of excited particles (sum of the red dotted value) and electrons absorbed in CAP [see Fig. 1(a)] equals the deficits in the electron numbers of the occupied states (blue dots). The number of excited electrons at E (see the left axis) and below E (see the right axis) at $t = 1.5$ fs after electron impact of 200 and 400 eV energies are given in Fig. 4(b). The inset is an enlarged view of the electron number at E with 200 eV incident energy. Most importantly and interestingly for comparison with experiments, we found the key profile of the excited spectrum that leads to the SE spectrum obtained in experiments as follows. Some of the SEs are absorbed in the CAP region with the rest of them still in the excited states just above the vacuum level energy, E_{v} at $t = 1.5$ fs. The excited electrons that distribute in the low-energy region up to $\sim$20 eV (inset) are emitted toward the vacuum as SE. The range of the energy

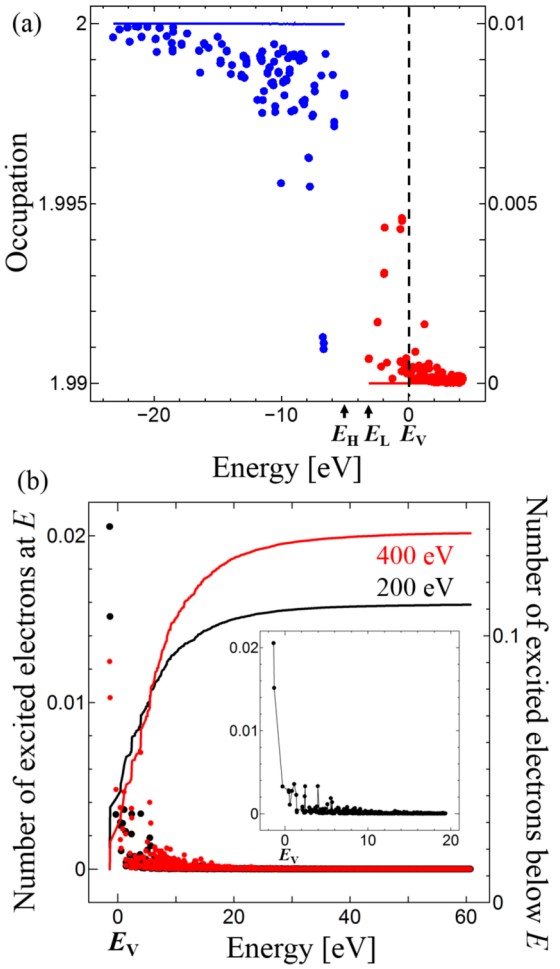

FIG. 4. (a) Snapshot of the electron occupation numbers of the target $C_{54}H_{18}$ at $t = 1.5$ fs after electron impact with kinetic energy of 200 eV. Here, spin degrees of freedom 2 is taken into account. Blue dots (see left axis) and red dots (see right axis) denote, respectively, the occupation numbers in the occupied and unoccupied KS levels that are separated by the HOMO-LUMO gap. E_{H}, E_{L}, and E_{V} indicate the energy of HOMO, LUMO, and the vacuum level, respectively. The vacuum level is set to zero and denoted by a dashed line. (b) Time-dependent number of excited electrons at E (dots) and below E (lines) of benzene at $t = 1.5$ fs. The black dots and curves show results for 200 eV incident electrons and the red dots and curves show that for 400 eV. The vacuum level (denoted by E_{V}) is set to zero. The data for 200 eV in the low energy region are replotted in the inset.

spectrum of SEs obtained here is compatible with typical ones observed in experiments [2–5], while the SEE of $C_{54}H_{18}$ and C_6H_6 [Fig. 4(b)] are of the order 0.1, which is substantially smaller than for those of ordinary substrates [11,12]. This is physically reasonable, because the target nanoflakes have fewer electrons to emit than the ordinary substrates. The substrate-dependent SEE properties are to be explored in the near future.

In conclusion, we have demonstrated the SEE dynamics by applying the TDDFT scheme to electron scattering with graphene-flake targets. We obtained the incident-electron energy dependence and bilayer effect on SEE, which are

interpreted by the scattering processes. The collective density oscillations of the target flake that emerge after SEE have a frequency specific to $C_{54}H_{18}$, independent of the initial kinetic energy of electron. The most important finding in our study is that the excitation dynamics responsible for SEE has been elucidated and that the energy spectrum of SE, which is consistent with typical properties observed in experiments, has been determined from first principles by utilizing the time-dependent KS decomposition scheme.

The authors wish to thank Y. Homma and H. Kato for valuable discussions about SEE. K.W. acknowledges partial financial support from MEXT through a Grant-in-Aid for Scientific Research (Grant No. 25400409). The numerical calculations were performed on the supercomputers at the Institute for Solid State Physics, University of Tokyo, and at the Research Center for Computational Science, National Institutes of Natural Sciences Okazaki Research Facilities.

[1] L. Austin and H. Starke, Ann. Phys. **314**, 271 (1902).
[2] H. Bruining, *Physics and Applications of Secondary Electron Emission* (McGraw-Hill Book Co., Inc., New York, 1954).
[3] R. E. Bunney, *Secondary Electron Emission*, Tech. Rep. (National Aeronautics and Space Administration, 1964).
[4] A. Modinos, *Field, Thermionic, and Secondary Electron Emission Spectroscopy* (Plenum Press, New York and London, 1984).
[5] M. Rösler, W. Brauer, J. Devooght, J.-C. Dehaes, A. Dubus, M. Cailler, and J.-P. Ganachaud, *Particle Induced Electron Emission I* (Springer Tracts in Modern Physics, 122) (Springer, Berlin Heidelberg, 1991).
[6] J. Ciston, H. G. Brown, A. J. D'Alfonso, P. Koirala, C. Ophus, Y. Lin, Y. Suzuki, H. Inada, Y. Zhu, L. J. Allen, and L. D. Marks, Nat. Commun. **6**, 7358 (2015).
[7] P. Tolias, Plasma Phys. Controlled Fusion **56**, 123002 (2014).
[8] J. S. Villarrubia, N. W. M. Ritchie, and J. R. Lowney, Proc. SPIE **6518**, 65180K (2007).
[9] A. R. Dzhanoev, F. Spahn, V. Yaroshenko, H. Lühr, and J. Schmidt, Phys. Rev. B **92**, 125430 (2015).
[10] A. C. Ferrari, F. Bonaccorso, V. Fal'ko, K. S. Novoselov, S. Roche, P. Boggild, S. Borini, F. H. L. Koppens, V. Palermo, N. Pugno, J. A. Garrido, R. Sordan, A. Bianco, L. Ballerini, M. Prato, E. Lidorikis, J. Kivioja, C. Marinelli, T. Ryhanen, A. Morpurgo, J. N. Coleman, V. Nicolosi, L. Colombo, A. Fert, M. Garcia-Hernandez, A. Bachtold, G. F. Schneider, F. Guinea, C. Dekker, M. Barbone, Z. Sun, C. Galiotis, A. N. Grigorenko, G. Konstantatos, A. Kis, M. Katsnelson, L. Vandersypen, A. Loiseau, V. Morandi, D. Neumaier, E. Treossi, V. Pellegrini, M. Polini, A. Tredicucci, G. M. Williams, B. Hee Hong, J.-H. Ahn, J. Min Kim, H. Zirath, B. J. van Wees, H. van der Zant, L. Occhipinti, A. Di Matteo, I. A. Kinloch, T. Seyller, E. Quesnel, X. Feng, K. Teo, N. Rupesinghe, P. Hakonen, S. R. T. Neil, Q. Tannock, T. Lofwander, and J. Kinaret, Nanoscale **7**, 4598 (2015).
[11] P. Riccardi, A. Cupolillo, M. Pisarra, A. Sindona, and L. S. Caputi, Appl. Phys. Lett. **101**, 183102 (2012).
[12] I. Montero, L. Aguilera, M. E. Dávila, V. C. Nistor, L. A. González, L. Galán, D. Raboso, and R. Ferritto, Appl. Surf. Sci. **291**, 74 (2014).
[13] A. Chvyreva and A. J. M. Pemen, IEEE Trans. Dielectr. Electr. Insul. **21**, 2274 (2014).
[14] E. Runge and E. K. U. Gross, Phys. Rev. Lett. **52**, 997 (1984).
[15] K. Burke, J. Werschnik, and E. K. U. Gross, J. Chem. Phys. **123**, 062206 (2005).
[16] C. A. Ullrich, *Time-Dependent Density-Functional Theory Concepts and Applications* (Oxford University Press Inc., New York, 2011).
[17] K. Tsubonoya, C. Hu, and K. Watanabe, Phys. Rev. B **90**, 035416 (2014).
[18] H. Zhang, Y. Miyamoto, and A. Rubio, Phys. Rev. Lett. **109**, 265505 (2012).
[19] P. Hohenberg and W. Kohn, Phys. Rev. **136**, B864 (1964).
[20] W. Kohn and L. J. Sham, Phys. Rev. **140**, A1133 (1965).
[21] M. Dauth and S. Kümmel, Phys. Rev. A **93**, 022502 (2016).
[22] U. De Giovannini, D. Varsano, M. A. L. Marques, H. Appel, E. K. U. Gross, and A. Rubio, Phys. Rev. A **85**, 062515 (2012).
[23] K. Yabana and G. F. Bertsch, Phys. Rev. B **54**, 4484 (1996).
[24] N. Troullier and J. L. Martins, Phys. Rev. B **43**, 1993 (1991).
[25] K. Kobayashi, Comput. Mater. Sci. **14**, 72 (1999).
[26] J. P. Perdew and A. Zunger, Phys. Rev. B **23**, 5048 (1981).
[27] D. E. Manolopoulos, J. Chem. Phys. **117**, 9552 (2002).
[28] T. Gonzalez-Lezana, E. J. Rackham, and D. E. Manolopoulos, J. Chem. Phys. **120**, 2247 (2004).
[29] A. Wasserman and K. Burke, in *Time-Dependent Density Functional Theory*, edited by M. A. L. Marques, C. A. Ullrich, F. Nogueira, A. Rubio, K. Burke, and E. K. U. Gross (Springer Berlin, 2006), p. 493.
[30] M. van Faassen, A. Wasserman, E. Engel, F. Zhang, and K. Burke, Phys. Rev. Lett. **99**, 043005 (2007).
[31] P. Bokes, F. Corsetti, and R. W. Godby, Phys. Rev. Lett. **101**, 046402 (2008).
[32] J-A. Yan, J. A. Driscoll, B. K. Wyatt, K. Varga, and S. T. Pantelides, Phys. Rev. B **84**, 224117 (2011).
[33] M. Lein and S. Kümmel, Phys. Rev. Lett. **94**, 143003 (2005).
[34] M. Thiele, E. K. U. Gross, and S. Kümmel, Phys. Rev. Lett. **100**, 153004 (2008).
[35] P. Elliott, J. I. Fuks, A. Rubio, and N. T. Maitra, Phys. Rev. Lett. **109**, 266404 (2012).
[36] C. A. Ullrich, U. J. Gossmann, and E. K. U. Gross, Phys. Rev. Lett. **74**, 872 (1995).
[37] M. Mundt and S. Kümmel, Phys. Rev. Lett. **95**, 203004 (2005).
[38] D. Hofmann, T. Körzdörfer, and S. Kümmel, Phys. Rev. Lett. **108**, 146401 (2012).
[39] We found in a preliminary calculation of impact of a classical point charge as a projectile at $C_{54}H_{18}$ that the SEE shows the maximum which is lower than the present one at around 100 eV. The details will be presented elsewhere.
[40] N. Yamamoto, C. Hu, S. Hagiwara, and K. Watanabe, Appl. Phys. Express **8**, 045103 (2015).
[41] S. A. Sato, Y. Shinohara, T. Otobe, and K. Yabana, Phys. Rev. B **90**, 174303 (2014).
[42] H. Hayashi and Y. Udagawa, in *Charged Particle and Photon Interactions with Matter: Recent Advances, Applications, and Interfaces*, edited by Y. Hatano, Y. Katsumura, and A. Mozumder (CRC, Boca Raton, 2011), p. 88.
[43] S. Karimi and C. A. Ullrich, Phys. Rev. B **90**, 245304 (2014).